Clim. Past Discuss., 8, 4223–4267, 2012
www.clim-past-discuss.net/8/4223/2012/
doi:10.5194/cpd-8-4223-2012

Climate of the Past Discussions

Variability of the ocean heat content during the last millennium – an assessment with the ECHO-g Model

P. Ortega[1,*], M. Montoya[1,2], F. González-Rouco[1,2], H. Beltrami[3], and D. Swingedouw[4]

[1]Dpto. Astrofísica y Ciencias de la Atmósfera, Facultad de Ciencias Físicas, Universidad Complutense de Madrid, Spain
[2]Instituto de Geociencias (UCM-CSIC), Madrid, Spain
[3]Climate and Atmospheric Sciences Institute/Department of Earth Sciences, St. Francis Xavier University, Antigonish, Canada
[4]LSCE/IPSL Laboratoire des Sciences du Climat et de l'Environnement, UMR8212, CEA-CNRS-UVSQ, Gif sur Yvette, France
[*]now at: Laboratoire des sciences du climat et de l'environnement, UMR8212, CNRS – LSCE/IPSL, CEA Saclay, Gif sur Yvette, France

Received: 30 July 2012 – Accepted: 13 August 2012 – Published: 30 August 2012

Correspondence to: P. Ortega (pablo.ortega@lsce.ipsl.fr)

Published by Copernicus Publications on behalf of the European Geosciences Union.

Abstract

Studies addressing climate variability during the last millennium generally focus on variables with a direct influence on climate variability, like the fast thermal response to varying radiative forcing, or the large-scale changes in atmospheric dynamics (e.g. North Atlantic Oscillation). The ocean responds to these variations by slowly integrating in depth the upper heat flux changes, thus producing a delayed influence on ocean heat content (OHC) that can latter impact on low frequency SST variability through reemergence processes. In this study, both the externally and internally driven variations of the OHC are investigated during the last millennium using a set of fully coupled simulations using the model ECHO-G. When compared to observations for the last 55 yr, the model tends to overestimate the global trends, and underestimate the decadal OHC variability. Extending the analysis back to the last one thousand years, the main impact of the radiative forcing is an OHC increase at high latitudes, explained to some extent by a reduction in cloud cover and the subsequent increase of short-wave radiation at the surface. This OHC response is dominated by the effect of volcanism in the preindustrial era, and by the fast increase of GHGs during the last 150 yr. Likewise, salient impacts from internal climate variability are observed at regional scales. For instance, upper temperature in the Equatorial Pacific is controlled by ENSO variability from interannual to multidecadal timescales. Also, both the Pacific Decadal Oscillation (PDO) and the Atlantic Multidecadal Oscillation (AMO) modulate intermittently the interdecadal OHC variability in the North Pacific and Mid Atlantic, respectively. The NAO, through its influence on North Atlantic surface heat fluxes and convection, also plays an important role on the OHC at multiple timescales, leading first to a cooling in the Labrador and Irminger seas, and later on to a North Atlantic warming, associated with a delayed impact on the AMO.

CPD
8, 4223–4267, 2012

1 Introduction

A manifest proof of anthropogenic influence on climate is the recent warming of the world oceans (Levitus et al., 2001), its prominent features being only reproduced by models when anthropogenic GHG forcing is considered (Levitus et al., 2001; Crowley et al., 2003; Gregory et al., 2004; Barnett et al., 2005; Delworth et al., 2005; Palmer et al., 2009). This positive trend in upper ocean temperature and heat content is robust to all the observational datasets and processing methods (Lyman et al., 2010; Trenberth, 2010). In the 20th century, two other prominent factors besides the GHG rise are known to have had a noticeable contribution to the global OHC integral. Both anthropogenic, and to a lesser extent, volcanic aerosols have partly offset the ocean warming resulting from increasing GHG concentrations (Delworth et al., 2005; Booth et al., 2012). Furthermore, the influence of volcanoes is particularly important to explain the observed decadal OHC changes (Domingues et al., 2008).

Observational estimates also report a flattening of the upper OHC trend since 2003, despite the steady increase in GHG concentrations and the subsequent radiative imbalance at the top of the atmosphere (Trenberth and Fasullo, 2010). This hiatus in the upper ocean warming is unrelated to changes in the external forcing and has been associated both with an increase of the Earth's outgoing radiation at the top of the atmosphere, partly associated with decadal El Niño variability, and secondly with an enhancement of heat transfer from the surface to deeper ocean levels (Katsman and van Oldenborgh, 2011; Meehl et al., 2011). The deeper ocean warming can be associated with a decrease in convection in the North Atlantic, which will diminish the vertical transfer of surface cold water thus leading to an anomalous warming at depth (Swingedouw et al., 2009). Furthermore, other internal processes of atmospheric and ocean variability have been proposed to influence OHC. Levitus et al. (2005), for instance, suggest a reversal of polarity in the PDO to explain the observed interdecadal OHC variability from 1956 to 2003. Also in the Pacific ocean, Willis et al. (2004) report a potential influence of strong ENSO-related events on the global OHC budget at interannual timescales. However, these latter analyses are prior to the identification of important instrumentation problems in the OHC estimates resulting, among other features, in an overestimation of its interdecadal variability (Levitus et al., 2009), and should be therefore confirmed in the new corrected climatologies (Domingues et al., 2008; Ishii and Kimoto, 2009; Levitus et al., 2009).

These assessments of natural and forced OHC variability are based on observations, representative only of the last 55 yr. A broader time perspective is therefore desirable, in particular for two reasons. First, the influence of internal modes of climate variability on the OHC can be assessed within a longer time period, thus allowing for a quantification of their associated global and local impacts at multidecadal to secular timescales. And second, further insight into the influence of external forcings can be achieved in an extended time interval that incorporates more volcanic eruptions and larger insolation changes, such as the transition from the Medieval Climate Anomaly (MCA) to the Little Ice Age (LIA). The aim of this study is therefore to improve our understanding of the processes and factors influencing OHC variability over the last millennium through the analysis of both control and forced millennial simulations with the ECHO-G model. An equivalent analysis, focused on the Atlantic meridional overturning variability, and making use of the same group of experiments is performed in Ortega et al. (2012, hereinafter referred to as OR12). Besides, in the current study a thorough comparison of the simulations with the available observations is carried out during the instrumental period (i.e. 1955–2010). In this way, the model performance is first assessed within the observational period before the impacts of the forcings and the influence of internal variability are evaluated from interdecadal to secular timescales. In the next Section the model and the experiments are presented, as well as the observational OHC dataset. Section 3 aims at determining the realism of the simulations by comparing them against the available evidence of past OHC variability (both observations and proxy reconstructions). The fingerprint of the external forcing on the global OHC is then addressed in Sect. 4. Likewise, Sect. 5 deals with the contribution of different

CPD
8, 4223–4267, 2012

modes of climate variability to global and local OHC. To conclude, Sect. 6 summarises and discusses the major findings of this study.

2 Simulations and instrumental data

2.1 Model description

Experiments were performed using the ECHO-G model (Legutke and Voss, 1999), which consists of the spectral atmospheric model ECHAM4 (Roeckner et al., 1996) and the ocean model HOPE-G (Wolff et al., 1997). The atmospheric component is characterized by a T30 horizontal resolution (ca. $3.75^{\circ} \times 3.75^{\circ}$), including 19 vertical levels. The horizontal resolution of the ocean model is about $2.8^{\circ} \times 2.8^{\circ}$, with an improvement of the meridional resolution from the Tropics towards the Equator to provide a better representation of equatorial and tropical ocean currents. In the vertical, the ocean has 20 variably spaced levels, 14 of which are located in the upper 1000 m. To avoid climate drift, the ocean component includes both heat and freshwater flux adjustments. Full details on the methodology applied for these flux corrections can be found in OR12.

2.2 Experimental setup

The same five ECHO-G simulations analysed and described in detail in OR12 were considered for this study: a 1000-yr present climate control simulation (CTRL), two forced runs covering the period 1000 to 1990 AD (FOR1 and FOR2), and two future scenario simulations (A2 and B2) that extend FOR1 until 2100 AD. FOR1 and FOR2 are driven by identical natural and anthropogenic forcing factors, only differing in their respective initial conditions. It should be remarked that the starting conditions in FOR1 are anomalously warm (Goosse et al., 2005; Osborn et al., 2006), thus introducing a noticeable initial trend in the OHC for several centuries, as it will become evident during the analysis. The implications of this drift will be later discussed. In the long forced simulations the influence of the forcing is represented by the changes in total solar irradiance, the effect of volcanic aerosols on the solar constant, and the concentrations of three greenhouse gases (CO_2, CH_4 and N_20), all these estimates based on reconstructions from Crowley (2000). For the climate change scenarios only the effect of GHG concentrations is considered, following the IPCC emission scenarios A2 and B2 (Nakicenovic et al., 2000), respectively. Time evolution of these three forcing factors is illustrated in Fig. 1 of OR12. Note that changes in anthropogenic aerosols and the vegetation cover are not represented in the model, both being expected to attenuate the industrial warming trends (Bauer et al., 2003; Osborn et al., 2006), and thereby the increase in OHC during the 20th and 21st centuries. Regarding the solar forcing, it should be mentioned that the reconstruction considered (Crowley, 2000) represents a change in total solar irradiance of 0.23 % from the Late Maunder Minimum to the present, comparatively larger than for new estimates employed in recent PMIP simulations which report a change below 0.1 % for the same transition (Schmidt et al., 2011). Further details on the model, the forcings and the experiments can be consulted in Zorita et al. (2004), González-Rouco et al. (2009) and OR12.

2.3 Observational and paleoproxy data

Observational estimates (OBS) of the ocean heat content are computed through gridded NODC-OCL temperature fields from the surface to 700 m depth (Levitus et al., 2012), covering the period 1955–2010. For the analysis of internal variability, several well-known climate indices, such as the NAO and ENSO will be employed. Observational series of all these indices were provided by the NOAA/OAR/ESRL PSD, Boulder, Colorado, USA (from http://www.esrl.noaa.gov/psd/data/climateindices/list/).

To our knowledge, there are no direct proxies for the OHC variability in the last millennium. However, records of past sea level (SL) can still provide a good benchmark to assess the realism of the initial trends in the simulations, since the thermosteric contribution to SL variability responds directly to changes in the OHC. For this task, a combination of SL observations since 1700 AD (from Jevrejeva et al., 2008a) and local paleoclimate reconstructions spanning the last two thousand years (from Kemp et al., 2011) will be employed.

3 Temporal evolution of ocean heat content and thermal expansion

This section describes the major aspects of OHC temporal variability, as represented by the ECHO-G simulations during both the instrumental period and the last thousand years. In each case, simulated variability is compared with the available instrumental and proxy evidence.

3.1 OHC variability in the instrumental period

Estimates of ocean heat content are calculated from global observations of upper ocean temperature. This computation requires reliable and globally distributed subsurface instrumental data, as well as the use of interpolation and regridding techniques. Since 1950, the spatial coverage of temperature measurements has improved as new data sources have become available (e.g. moored buoys, ARGO floats, bathythermograph measurements; Boyer et al., 2009). The integration of these data is subject to important uncertainties, since it is sensitive to the records considered and the different methodologies applied, such as the mapping and bias correction techniques (Gregory et al., 2004; Lyman et al., 2010). This has lead to the publication of somewhat different OHC estimations by different groups and institutions (Domingues et al., 2008; Ishii and Kimoto, 2009; Levitus et al., 2009), the major discrepancies concerning the representation of interannual OHC variability (Lyman et al., 2010).

Our analysis will be therefore focused on the long-term trends, and the representation of decadal OHC variability. As for the observational records, the simulated OHC anomalies are computed in the upper 700 m of the ocean. Also, for a better comparison among the basins and the global ocean, the corresponding anomalies are calculated as heat content changes by unit area (Fig. 1). To cover the whole observational period (1955–2010) with the forced simulations, the first 20 yr of the future scenario runs are shown after 1990. Note that OHC oscillates within the range of CTRL variability (dashed horizontal lines in Fig. 1) from 1955 to 1990, and goes beyond these values afterwards. Since A2 and B2 assume zero volcanic activity and keep solar irradiance constant from year 1990 AD, they both miss the natural external influences. In order to take into account a more recent history of these forcings, FOR1 has been extended to year 2000, now also including the influence of Pinatubo's eruption (in 1991 AD). The corresponding variations in the different radiative forcings are also shown to shed light on their particular role throughout the instrumental period (Fig. 1e). Globally, forced simulations are able to partly reproduce the low-frequency OHC modulation in observations associated with the cooling effect of volcanoes. Both simulations and observations evidence that most decadal variability occurs in the Pacific and Indian oceans, while the Atlantic ocean warms almost linearly. Discrepancies in decadal variability among FOR1, FOR2 and OBS (blue, green and black curves in Fig. 1) point to potential influences of natural climate variability in the Pacific and Indian basins, superimposed to the GHG-driven trend and the volcanic modulation. The global integral shows better agreement since local effects are partly canceled out. Overall, the forcing explains about 70 % of the simulated and observed total OHC variance, either globally or by basins (Table 1). However, the large variance explained is mainly related to the steep warming trend after year 1990.

Observed and simulated trends are now compared separately before and after 1990 (Table 2). All forced simulations overestimate the global OHC trends, especially from 1955 to 1990, the period with largest observed decadal OHC variability. This overestimation can be arguably attributed to the lack of sulphate aerosols in the forced simulations, that can offset the GHG warming up to a 50 % (Delworth et al., 2005). By basins, trends are mostly overestimated in the Pacific (that dominates the warming due to its larger extension) and Indian oceans, and show a good agreement in the Atlantic (Fig. 1b–d and Table 2), probably indicating that internal variability in this basin

CPD
8, 4223–4267, 2012

compensates the offset due to the missing contributions from changes in anthropogenic aerosols and the vegetation cover.

Spatial distribution of recent trends is now explored. In the period 1955–1990 (Fig. 2, left column), a weak general warming is observed in the three datasets, subject to local influences in the Atlantic and Pacific oceans, that differ between the simulations and the observations. From 1991 to 2010 (Fig. 2, middle column), some robust features can be highlighted both in the observed and simulated trends, with larger tendencies in the North Atlantic and western Pacific, and a rather uniform warming in the Indian basin. Note that observations show opposite trends in both the Atlantic and Pacific oceans with respect to the first period, that could be compatible with shifts in the phases of the PDO and the AMO indices among both periods. These contributions of natural variability will be further analysed in Sect. 5. Finally, during the last 90 yr of the scenario runs (Fig. 2, right column) a worldwide warming pattern emerges, with larger trends at high latitudes of the Northern Hemisphere. Yet, the local cooling south of Greenland persists, in line with a local decrease in deep convection that would reduce the downward heat transport. This reduced convection is also compatible with the reported weakening of the AMOC cell in future scenario simulations (Schmittner et al., 2005).

Previous results suggest both a predominant influence of the forcing, most important from 1990, along with some impact of internal climate variability, able to produce important OHC changes at least at local scales. These results are however limited by the short time span of the observational period. The use of the millennial simulations will allow for a better understanding and quantification of these influences. In a first step, simulated OHC variability will be assessed for the last millennium.

3.2 Thermosteric sea level and ocean heat content throughout the last millennium

Ocean heat content, when integrated over deep ocean levels, is a good indicator of decadal changes in the radiation balance at the top of the atmosphere (Palmer et al., 2011). However, the deep ocean is not always in full thermal equilibrium, as it requires several millennia to reach steady conditions and fully-coupled simulations are limited by the high computational cost. These potential instabilities in the deeper ocean can partially mask the oceanic response to the radiative forcing. In fact, the ECHO-G simulations show important temperature trends at intermediate and bottom waters (Fig. 3). These trends are more prominent in FOR1, whose ocean starts anomalously warm at 1000 m depth. Additionally, CTRL shows opposite and long-lasting trends above and below 2000 m, a probable indicator of a persistent drift in the model. For the rest of the analysis these steady temperature trends in CTRL are removed at each ocean level from all the simulations.

OHC in the upper 700 m shows a comparable evolution in FOR1 and FOR2 since 1700 AD (Fig. 4a), while substantially smaller variability occurs in CTRL (dotted black line). Prior to this year, FOR1 is clearly influenced by its warm starting conditions. Indeed, its initial OHC700 cooling trend cannot be explain in terms of the changes in the radiative forcing (Fig. 4a, d). This problem is not present in FOR2, for which both curves have a large degree of coherence throughout the whole length of the simulation. Therefore, from now on, analyses covering the last millennium will be only addressed with FOR2. FOR1, together with the scenario simulations, will be left for analyses centered on the observational period, during which the effect of initial drift becomes negligible.

Given the lack of direct paleo-evidence of past OHC variability, the records of SL variability are used instead as a reference for the simulations. They are compared with the simulated thermal expansion in the different experiments, as the rest of contributions, such as the melting of land glaciers and polar ice caps, are not represented by the model. Since the ocean component of ECHO-G has a fixed volume, thermal expansion is computed indirectly as in Gregory and Lowe (2000), by assuming a constant water mass and calculating the corresponding volume change through time.

This thermosteric component shows a remarkably strong initial drift (Fig. 4b), fueled by the trends in the deeper ocean. Part of this drift can be corrected by comparing with the SL data. The longest instrumental SL record is computed from tide gauge observations since 1700 AD (Jevrejeva et al., 2008a, hereafter Jev08). These estimates show

Discussion Paper | Discussion Paper | Discussion Paper | Discussion Paper |
CPD
8, 4223–4267, 2012

evidence that acceleration of sea level rise began about 200 yr ago, and was preceded by a century of comparatively flattened SL variations (brown line in Fig. 4c). A local reconstruction from salt-marsh sediments in North Carolina (Kemp et al., 2011, hereafter Kemp11) is in broad agreement with estimates in Jev08, and shows stable SL variability in the same period. This record is summarised in an idealised manner by the yellow filled curve in Fig. 4c. It is therefore plausible that all components of sea level rise (SLR), and in particular the thermal expansion, leveled off during the 18th century. This assumption is now applied to propose a correction for the effect of initial trends in the later centuries of the forced runs. Both simulations are detrended by removing their corresponding trends in the period 1800–1900, which now becomes flattened as in the reconstructions. In this way, the rate of observed SLR and simulated thermal expansion can be compared in the last two centuries.

Before the 17th century, both the simulated thermal expansion and the SL proxies of Kemp11 show comparable downward trends from 1500 onwards, but exhibit a clear mismatch in the earlier centuries. Indeed, proxies show evidence of a steady SLR since 1000 AD while the forced simulations indicate a sustained decrease in thermal expansion. None of these trends is observed in our estimates of the total radiative forcing (Fig. 4d). It should be kept in mind that the SL curve shown for Kemp11 is idealised, and represents local changes in North Carolina. It is not clear to what extent this proxy represents the global SL changes. Likewise, the analysis suggest that in the simulations the effect of the initial trends is still noticeable before 1700 AD.

Regarding the last two centuries, for which this effect has been corrected, simulated thermal expansion only accounts for about a sixth of the observed sea level rise (Table 3). It is not clear, however, if this contribution is underestimated by the model. While some observational studies suggest a leading contribution from thermal expansion on sea level (Bindoff et al., 2007; Domingues et al., 2008), others point to a dominant role of melting processes (Miller and Douglas, 2004; Jevrejeva et al., 2008b). In the period 1955–2000 of the ECHO-G simulations, thermal expansion would account for a third of the recent observed sea level rise (Table 3). This trend is notably overestimated by the

CPD
8, 4223–4267, 2012

model since it is almost twice as large as the trend for the observed thermal expansion (computed from temperatures in OBS), partly due to the missing contribution of anthropogenic aerosols. During the scenario simulations, the rate of thermal expansion is accelerated by about a factor of three with respect to the period 1955–2000 (Table 3). Although the corresponding trend for the SLR cannot be estimated by the model, the evaluation for the 19th and 20th centuries suggested a thermosteric contribution of about one sixth. This result, however, is difficult to reconcile with future projections in the fourth IPCC assessment report (Meehl et al., 2007), in which thermal expansion is expected to explain 70 to 75 % of the total sea level rise by the end of the 21st century. In order to improve our understanding on the direct role of ocean warming to SLR, the mass increase due to land-ice melting needs to be better constrained.

4 Fingerprint of external forcing on ocean heat content

As deeper ocean levels show larger drifts in temperature (Fig. 3) the analysis will keep focused on the upper 700 m. At this depth, the OHC (hereinafter referred as OHC700) shows a good correspondence with variations in the net radiative forcing (Fig. 4). The main aspects of this influence are now discussed.

4.1 Quantifying recent forcing impacts

The last 55 yr have witnessed relevant changes in the radiative forcing, mainly associated with an acceleration of both GHG and sulphate aerosols emission rates and the occurrence of three major volcanic eruptions (Mt. Agung in 1963; El Chichón in 1983 and Pinatubo in 1991) and five complete solar cycles. In response to these changes, the world ocean has experienced a remarkable warming trend, modulated to some extent at decadal timescales (Fig. 1). In this context, however, impact and attribution studies are constrained by the short time span of the observational records. Particular caution should be taken since physically unrelated quantities can coincidentally vary at

CPD
8, 4223–4267, 2012

comparable timescales. We now assess the relation between the external forcing and upper OHC both in the observations and the model. To ensure that no artificial relationship emerges in our regression analyses, a statistical significance test is employed that takes into account the serial autocorrelation to correct for the effective sample size (Bretherton et al., 1999).

In order to maximise the signal of the oceanic response, the analysis in the observational period is exclusively focused on the effect of the total radiative forcing. The period considered for the analysis is 1955–2000, to include the latest changes in solar and volcanic forcing used for the extended FOR1 run. Figure 5 shows the regression patterns between the total radiative forcing in this experiment (black line in lower panels of Fig. 1) and the observed and simulated OHC700 global fields. Both plots exhibit an overall warming pattern and some noticeable local coolings. Yet, there is a general disagreement in the regions where these changes are significant. However, this calculation can be affected by the absence of anthropogenic aerosols in the simulations, which may be crucial to explain recent decadal changes in North Atlantic climate (Booth et al., 2012). The validity of these results will be assessed in next section by extending the analysis to the whole FOR2 run. This will allow to provide further insight on the role of each forcing factor.

4.2 Influence of the forcing in the last thousand years.

Within the last millennium, the pattern of response to an increase in the total radiative forcing (Fig. 6a) corresponds to a generalised warming of the upper ocean, with larger values in the extratropics, and some local coolings in regions of deep water formation, like the Labrador and Weddell Seas. Unlike in the observational period, most of these changes are significant, especially northward of 40° S.

Considering the individual effect of different factors, only the GHGs exhibit a widespread impact. In particular, they have a significant effect in the Tropics (Fig. 6b) and the convection regions, being also associated with the largest regression coefficients. In contrast, the fingerprint of solar variability (Fig. 6c) is characterized by a mild

CPD
8, 4223–4267, 2012

response mainly localised at midlatitudes in the three major basins. Regression values with the effective solar constant (Fig. 6d) are considerably lower, as it is also punctuated by the episodic influence of volcanic eruptions, which is clearly not linear. The impact of volcanoes is thus evaluated through a composite analysis focused on the top 25 and 10 preindustrial eruptions, to distinguish the moderate and strong impacts. Composite maps are calculated by averaging the differences in OHC700 occurring between the 5 yr following and the 5 yr preceding the selected volcanic eruptions, and their significance is assessed by comparing with the 2.5 and 97.5 percentiles of a Monte Carlo ensemble consisting of 1000 analogous differences in CTRL. As for the solar irradiance, the largest OHC700 changes take place in the extratropics (Fig. 6e–f). The pattern of cooling is similar in both composite analyses, with no remarkable spatial differences. As expected, larger negative anomalies are observed for the strongest eruptions (Fig. 6f).

The contribution of heat fluxes at the surface and cloud coverage is now analysed to help us understand the reasons for both the different latitudinal OHC700 response to the forcing and the larger sensitivity in the extratropics. This is done by calculating their respective linear regressions with the total radiative forcing (Fig. 7). Regarding the cloud coverage, the main changes associated with a RF increase consist of a general cloud reduction at extratropical latitudes and a remarkable increase over the Ross Sea (Fig. 7a). A similar pattern, but with opposite sign, characterizes the changes in shortwave radiation (Fig. 7b), as it responds inversely to variations in cloud albedo. At midlatitudes cloud cover decreases leading to increased solar radiation at the surface, while in the deep water formation regions the incoming radiation is reduced in response to a larger cloud fraction. In the Southern ocean these latter changes are counterbalanced by opposite contributions of the other heat flux components (Fig. 7c–e). Also of note is a weak but widespread surface warming related to changes in long-wave radiation (Fig. 7c), and a notable ocean heating across the Gulf Stream and subpolar gyre responding to both latent and sensible heat flux changes (Fig. 7b, c).

Adding up all the different influences (Fig. 7f), there is a worldwide net surface warming following the increases of the RF, with larger values in the regions of ocean deep convection and also in the extratropics. In the deep water formation regions the radiatively-forced surface warming reduces convection activity through its effect on ocean stratification. As a result, the upper ocean experiences a net cooling, as was observed in Fig. 6a. In the rest of the ocean the warming is observed both at the surface and integrated in depth, the OHC700 increase being therefore related to the downward penetration of the net positive heat flux into the ocean. Note that this larger response at midlatitudes is partly linked to a local increase of solar radiation at the surface following a significant reduction in cloud coverage. This particular pattern is not observed for the other surface heat fluxes.

We turn now our attention to the temporal features associated with the influence of the different radiative forcings. A wavelet coherence analysis (Torrence and Webster, 1999) is used to investigate the common spectral features between the OHC700 and the different forcings throughout the last millennium (Figs. 8 and 9). For all practical purposes, wavelet coherence can be regarded as a localized correlation coefficient but in time frequency space (Grinsted et al., 2004). Besides, to help in the interpretation of potential causality between the different variables, phase-relationship at each time and frequency is also computed. In-phase relationships are represented by eastward arrows in the wavelet coherence plots.

The total equivalent radiative forcing shows a high degree of coherence with OHC700 variability at all timescales (Fig. 8), with changes in the forcing always leading (since arrows have a small northward component) the heat content variations. In the preindustrial period, most of the coherence comes from volcanoes, as highlighted by the good agreement between Figs. 8 and 9a. Note that coherence at interannual timescales is only present when the radiative forcing is punctuated by the effect of volcanism, as variations in solar irradiance and GHGs occur at longer scales. Moreover, the influence of volcanic aerosols is also relevant at lower-frequencies. Strong volcanoes impact as a step down signal on the OHC700 curve (Fig. 9a, upper panel), as it has been already

CPD
8, 4223–4267, 2012

described in other forced simulations (Gleckler et al., 2006; Gregory et al., 2006; Gregory, 2010). This signal, integrated during periods of intense volcanism (e.g. 1150 to 1300 AD or 1550 to 1700 AD), can impact the OHC700 variability at multidecadal and even secular timescales. Likewise, solar variability (Fig. 9b), shows some intervals of common variance with the OHC700 at interdecadal timescales. Finally, regarding the slowly-varying GHGs, high coherence arises at secular timescales during the last few centuries of the millennium, and at higher frequencies after the onset of the industrial era (Fig. 9c).

So far, the analysis has been centred on the instantaneous OHC700 response to the external forcing factors. Correlations in Fig. 10 illustrate their influence at other lags. For the total radiative forcing, significant correlations are found for lead times from 50 to 0 yr, and maximum values when it leads the OHC700 changes by 1–2 yr. This maximum impact is associated with the short-lived influence of volcanoes (blue line). In contrast, the slowly varying solar and GHG forcings show maximum correlations for lead times of 20 and 70 yr, respectively. This delayed response points to a gradual accumulation of the energy going into the ocean, the lag timescale being therefore set by slow vertical diffusion processes.

It has been shown that at higher-frequencies, and in particular at interannual timescales, coherence with the radiative forcing is limited (Fig. 8) and only the volcanic forcing can explain some OHC700 variability. Hence, this is the range of frequencies at which internal variability is bound to account for a larger fraction of OHC700 variability. The next section develops a comprehensive analysis of these potential impacts.

5 OHC imprints of internal climate variability

5.1 Influence of internal variability over the last 55 yr

Previous sections suggest a potential role of internal modes of variability to locally modulate the upper ocean warming trends in the observational period. Globally, internal climate variability has been proposed to explain part of the interannual OHC700 changes during the last millennium, especially during periods of low volcanic activity. Other works also support the influence of different modes of climate variability on the OHC700. For example, there is particular evidence that ENSO-related variability has produced noticeable interannual OHC700 changes during the observational period (Willis et al., 2004). Thereby, other climate modes involving large-scale SST changes, such as the AMO or the PDO, can also potentially affect, locally or globally, the OHC700 budget. It is also known that predominant atmospheric patterns, such as the NAO, can locally alter the air-sea heat fluxes at the ocean surface and trigger deep convection events (Pickart et al., 2003), thus also contributing to heat exchange with the deeper ocean.

A first evaluation of the influence of modes of climate variability on the observed and simulated OHC700 is performed in the whole instrumental period (e.g. 1955–2010). For this analysis, the NAO and three well-known modes of SST variability are explored, namely, ENSO (represented by El Niño 3.4 index), PDO and AMO. In the forced simulations, the climate indices are calculated following the same definitions as for the observations. ENSO corresponds to El Niño 3.4 index, defined as the mean SST value from 5° S to 5° N and 170° to 120° W (Trenberth, 1997). The PDO index is derived as the leading PC of monthly SST anomalies in the North Pacific Ocean, poleward of 20° N (Mantua et al., 1997). And finally, the AMO is defined as the detrended average of Atlantic SST anomalies north of the Equator (Enfield et al., 2001). For the calculation of all these three indices, the local SST anomalies are calculated with respect to the global SST mean, thus filtering out the influence of the global warming signal and only representing the internal natural variability (Zhang et al., 1997). Finally, the NAO is calculated as the leading mode of SLP anomalies in the North Atlantic (Wallace and Gutzler, 1981).

The corresponding OHC700 fingerprints are illustrated in the regression patterns of Fig. 11. Both the observed ENSO and PDO indices exhibit similar patterns, with the former showing stronger equatorial anomalies, and the latter larger impact in the North

CPD
8, 4223–4267, 2012

Pacific. Generally, both patterns are associated with an eastern warming and a western cooling of the upper Pacific ocean that could explain the local shift in OHC700 trends from 1955–1990 to 1991–2010 (see Fig. 2). In contrast, in the model the zonal dipole structure is only observed at the Equator for the ENSO index, and at the North Pacific for the PDO, suggesting that the model cannot capture the coupling between both modes (Newman et al., 2003). Regarding the AMO, it relates in the observations to positive OHC700 anomalies over the whole Atlantic, but shows no significant changes in FOR1+A2. This probably indicates that, given the limited time period, no relevant changes of this index are taking place in the simulations. Finally, the most significant impact of the NAO is a cooling over the Labrador and Irminger Seas in the observations, partly reproduced in the simulations. This cooling is likely responding to changes in convection, which is also affected by the NAO over both regions (Dickson et al., 1996; Pickart et al., 2003). Besides, an OHC700 increase is simulated at midlatitudes, similar to the one already described in response to the radiative forcing (Fig. 6). Therefore, this imprint is more probably associated with the recent changes in the forcing, which may be also having an impact on NAO variability. Indeed, the final tendency to negative NAO values in the observations can explain the remarkable warming of the North Atlantic since year 1990 (see Fig. 2). The analysis is on the following extended to the last thousand years, to better determine the spatial impacts associated with the previous modes and the predominant timescales of their influence.

5.2 Modes of climate variability and OHC in the last millennium

The regression patterns in Fig. 11 are now calculated for the complete FOR2 simulation (Fig. 12). The patterns corresponding to ENSO and the PDO are similar to those described during the observational period. Besides, the AMO is now related to a general warming in the North Atlantic, more in line with the OHC700 pattern described for the observations. It also shows a local cooling in the Labrador Sea and some positive OHC700 anomalies in the North Pacific, near the region where the PDO occurs. Similar features are also observed in the pattern of the NAO (Fig. 12d). This suggests a

CPD
8, 4223–4267, 2012

link between the three modes in the model. Indeed, the AMO is known to be related to changes in the AMOC (Knight et al., 2005), the latter being driven by changes in the NAO in the forced simulations (Ortega et al., 2012). Also, the interrelationship between the NAO and the Arctic Oscillation (AO) may explain an atmospheric influence over the North Pacific, and thereby on the PDO. The lead-lag relationship at low-frequencies between the previous indices in the model is explored in Fig. 13. The NAO leads the AMO and PDO changes by 2 and 4 yr, respectively. Furthermore, the radiative forcing is found to have a leading role on the NAO, which lags the total RF changes by about 1 yr.

The influence of these modes in the OHC700 variations is now explored in a temporal and spectral perspective. For this, a wavelet coherence analysis is again employed (Fig. 14). In the previous analysis of the forcings, that have a worldwide impact on the OHC700, the coherence was established with respect to the global OHC700 integral. In this case, however, the different modes produce more localised influences, and thereby coherence is investigated regionally. Each index is compared with the OHC700 average in the region where its influence is originally taking place (dotted rectangles in Fig. 12). Note that OHC variability in these four regions (dark curves in top panels of Fig. 14) still presents a modulation by the external forcing at the very lowest frequencies (beyond centennial). Yet, they also exhibit other predominant scales of variability at higher frequencies, which are potentially attributable to the local modes. For ENSO, both time-series (i.e. El Niño 3.4 and the OHC700 average in the Equatorial Pacific) show a high degree of coherence at interannual timescales, and also relative good agreement from decadal to multidecadal timescales. Although in some particular periods (e.g. 1100–1300) coherence is damped above decadal timescales, overall ENSO explains most of OHC700 variability over the equatorial Pacific. Regarding the PDO and AMO, both indices show alternating periods of good and poor coherence with the local OHC700 at multidecadal timescales. The fact that the phase of the relationships (arrows in Fig. 14) remains stable throughout the whole simulation, with westward arrows in Fig. 14b accounting for a North Pacific cooling and eastward arrows in Fig. 14c representing a

CPD
8, 4223–4267, 2012

mid-latitude North Atlantic warming, both compatible with the corresponding OHC700 patterns in Fig. 12, points to a real but intermittent modulation of the OHC700 by both indices. The reasons for this discontinuous influence are not clear to us, although some impact of the radiative forcing cannot be excluded. Indeed, Fig. 6 showed that OHC700 in both regions, unlike in the equatorial latitudes, is particularly sensitive to changes in the radiative forcings. There is also the possibility that other modes of variability are masking part of the signal. Finally, the NAO shows a good degree of coherence with interannual and interdecadal OHC700 variability in the Labrador Sea, although subject again to some periods of intermittence. Interestingly, the phase of this relationship changes at different timescales. For periods up to 30 yr, the westward arrows indicate a direct association between the NAO and a cooling over the Labrador Sea, as expected given the leading role of the NAO on both North Atlantic convection and the AMOC discussed in OR12. Besides, at longer timescales some periods (e.g. 1300–1500) give evidence of the opposite relationship. As the NAO has been found to respond to variations in the total radiative forcing (Fig. 13), the Labrador warming observed at low frequencies could be actually attributed to a direct OHC response to this forcing.

6 Conclusions

The upper OHC response to the external forcing as well as the fingerprint of several modes of climate variability have been assessed in a suite of observations and model simulations covering the period 1000 to 2100 AD.

In the instrumental period, the model overestimates the warming trend and underestimates the decadal OHC variability. The misrepresentation in trends is explained to some extent by the lack of sulphate aerosols in the simulations, whose cooling effect is known to partially offset the GHG-driven warming (Delworth et al., 2005). Note that aerosols have also been proposed to be a main contributor to North Atlantic decadal variability over the last century (Booth et al., 2012). The spatial distribution and intensity of the upper warming trends have changed from 1955–2010 to 1991–2010.

CPD
8, 4223–4267, 2012

These changes respond, respectively, to a sustained increase of the net radiative forcing (mostly associated with an acceleration of GHG emissions) and a shift in the values of the PDO and AMO indices.

During the last millennium, the simulated OHC is subject to the effect of a drift associated with the starting conditions. To assess the importance of these trends, the simulations have been compared with several reconstructions of SL variability, the only proxy available with a direct relationship with the OHC. Since the model is not able to reproduce the changes in the melting of land-ice sheets, only the thermosteric component has been considered. The comparison with the SL proxies has allowed for a drift correction since year 1700. Besides, the model suggests that thermal expansion has only contributed to one sixth of the total observed sea level rise in the last 200 yr. Also, to minimise the effect of the drift, the subsequent analysis concerning the OHC throughout the last millennium is focused on the upper 700 m of the FOR2 simulation.

The spatial imprint of the radiative forcing was also analysed. All the individual forcings show a similar impact, with larger effect at extratropical latitudes. This larger response at midlatitudes is partly explained by a local reduction in cloud cover, thus allowing a larger fraction of solar radiation to reach the ocean surface. Other contributions to the net surface heat flux, such as the outgoing longwave radiation or the sensible and latent heat fluxes do not reproduce this different latitudinal response. In the preindustrial era, a large part of the forced OHC variability is associated with volcanism, with some solar contribution at interdecadal timescales (periods from 10 to 30 yr). After 1850, low-frequency OHC variability is mainly responding to the increased GHG concentrations, and the influence of volcanic activity remains important at decadal and intradecadal timescales. Interestingly, the ocean shows a delayed response to all the radiative forcings, with the largest impacts occurring about 2, 20 and 70 yr after the changes in volcanic, solar and GHG forcing, respectively.

Finally, the contributions from four large-scale modes of climate variability have been explored (i.e. ENSO, the PDO, the AMO and the NAO). As their influence on the OHC is mainly local, their spectral features have been directly analysed in their respective

CPD
8, 4223–4267, 2012

centers of action. In these four regions the long-term OHC variations still exhibit some modulation by the external forcing. Yet, at shorter timescales (annual to secular) the regions show periods of spectral coherence with their corresponding climate indices. The influence of ENSO is mainly localised in the Equatorial Pacific, where it is found to dominate the local OHC variability from interannual to multidecadal timescales. This predominant role of ENSO to drive local OHC variability at all timescales is in line with a major contribution of internal variability in the Tropics, and a largest impact of the external forcing at extratropical latitudes. Likewise, positive PDO and AMO indices relate respectively to a cooling in the North Pacific, and warming at midlatitudes in the North Atlantic, both modes contributing discontinuously to OHC variability at multi-decadal timescales. The NAO, in the model and observations, produces a cooling over the Labrador Sea, that in the simulations gives rise to a strengthening of the AMOC cell. This impact takes place from interannual to interdecadal timescales. To conclude, the fact that natural modes of climate variability, such as ENSO, PDO or AMO can impact the OHC globally or locally is important for the coming decades, since they can temporarily mitigate or intensify the ocean warming signal, and they can modulate as well the regional sea level rise.

Acknowledgements. All this work has been possible thanks to the funding by the MCINN projects CGL2005-06097 and CGL2008-06558-C02-C01/CLI, and the MARM project 200800050084028. We are grateful to A. Grinsted and S. Jevrejeva for making the MatLab wavelet coherence package and their global sea level reconstructions available, and also to A. Kemp for kindly sharing the data from North Carolina with us.

The publication of this article is financed by CNRS-INSU.

CPD

8, 4223–4267, 2012

Title Page
Abstract | Introduction
Conclusions | References
Tables | Figures
◀| |▶
◀ ▶
Back | Close
Full Screen / Esc
Printer-friendly Version
Interactive Discussion

References

Barnett, T. P., Pierce, D. W., Achuta Rao, K. M., Gleckler, P. J., Santer, B. D., Gregory, J. M., and Washington, W. M.: Penetration of Human-Induced Warming into the World's Oceans, Science, 309, 284–287, 2005. 4225

Bauer, E., Claussen, M., Brovkin, V., and Huenerbein, A.: Assessing climate forcings of the earth system for the past millennium, Geophys. Res. Lett., 30, 1276, doi:10.1029/2002GL016639, 2003. 4228

Bindoff, N., Willebrand, J., Artale, V., Cazenave, A., Gregory, J., Gulev, S., Hanawa, K., Le Quere, C., Levitus, S., Nojiri, Y., Shum, C., Talley, L., and Unnikrishnan, A.: Observations: oceanic climate change and sea level. Climate change 2007: The Physical Science basis Contribution of Working Group I to the Fourth Assessment Report of the Intergovernmental Panel on Climate Change, edited by: Solomon, S., Qin, D., Manning, M., Chen, Z., Marquis, M., Averyt, K. B., Tignor, M., and Miller, H. L., Cambridge University Press, Cambridge, 385–432, 2007. 4233

Booth, B. B. B., Dunstone, N. J., Halloran, P. R., Andrews, T., and Bellouin, N.: Aerosols implicated as a prime driver of twentieth-century north atlantic climate variability, Nature, 484, 228–232, doi:10.1038/nature10946, 2012. 4225, 4235, 4242

Boyer, T., Antonov, J., Baranova, O., Garcia, H., Johnson, D., Locarnini, R., Mishonov, A., O'Brien, T., Seidov, D., Smolyar, I., and Zweng, M.: World ocean database 2009, edited by: Levitus, S., NOAA Atlas NESDIS, Vol. 66, US Gov. Printing Office, Washington DC, 216 pp., DVDs, 2009. 4229

Bretherton, C., Widmann, M., Dymnikov, V., Wallace, J., and Bladé, I.: The effective number of spatial degrees of freedom of a time-varying field, J. Climate, 12, 1990–2009, 1999. 4235

Crowley, T. J.: Causes of climate change over the past 1000 years, Science, 289, 270–277, 2000. 4228

Crowley, T. J., Baum, S. K., Kim, K. Y., Hegerl, G. C., and Hyde, W. T.: Modeling ocean heat content changes during the last millennium, Geophys. Res. Lett., 30, 1932, doi:10.1029/2003GL017801, 2003. 4225

Delworth, T. L., Ramaswamy, V., and Stenchikov, G: The impact of aerosols on simulated ocean temperature and heat content in the 20th century, Geophys. Res. Lett., 32, L24709, doi:10.1029/2005GL024457, 2005. 4225, 4230, 4242

Dickson, R., Lazier, J., Meincke, J., Rhines, P., and Swift, J.: Long-term coordinated changes in the convective activity of the North Atlantic, Prog. Oceanogr., 38, 241–295, 1996. 4240

Domingues, C. M., Church, J. A., White, N. J., Gleckler, P. J., Wijffels, S. E., Barker, P. M., and Dunn, J. R.: Improved estimates of upper-ocean warming and multi-decadal sea-level rise, Nature, 453, 1090–1093, doi:10.1038/nature07080, 2008. 4225, 4226, 4229, 4233

Enfield, D., Mestas-Nunez, A., and Trimble, P. J.: The Atlantic multidecadal oscillation and its relation to rainfall and river flows in the continental U.S., Geophys. Res. Lett., 28, 2077–2080, 2001. 4239

Gleckler, P., Achuta Rao, K., Gregory, J., Santer, B., Taylor, K., and Wigley, T.: Krakatoa lives: The effect of volcanic eruptions on ocean heat content and thermal expansion, Geophys. Res. Lett., 33, L17702, doi:10.1029/2006GL026771, 2006. 4238

González-Rouco, J. F., Beltrami, H., Zorita, E., and Stevens, M. B.: Borehole climatology: a discussion based on contributions from climate modeling, Clim. Past, 5, 97–127, doi:10.5194/cp-5-97-2009, 2009. 4228

Goosse, H., Crowley, T., Zorita, E., Ammann, C., Renssen, H., and Driesschaert, E.: Modelling the climate of the last millennium: What causes the differences between simulations?, Geophys. Res. Lett., 32, L06710, 2005. 4227

Gregory, J.: Long-term effect of volcanic forcing on ocean heat content, Geophys. Res. Lett., 37, L22701, doi:10.1029/2010GL045507, 2010. 4238

Gregory, J. M. and Lowe, J.: Predictions of global and regional sea-level rise using aogcms with and without flux adjustment, Geophys. Res. Lett., 27, 3069–3072, 200. 4232

Gregory, J. M., Banks, H. T., Stott, P. A., Lowe, J. A., and Palmer, M. D.: Simulated and observed decadal variability in ocean heat content, Geophys. Res. Lett., 31, L15312, doi:10.1029/2004GL020258, 2004. 4225, 4229

Gregory, J. M., Lowe, J. A., and Tett, S. F. B.: Simulated global-mean sea level changes over the last half-millennium, J. Climate, 19, 4576–4591, 2006. 4238

Grinsted, A., Moore, J., and Jevrejeva, S.: Application of the cross wavelet transform and wavelet coherence to geophysical time series, Nonlinear Proc. Geoph., 11, 561–566, 2004. 4237

Ishii, M. and Kimoto, M.: Reevaluation of historical ocean heat content variations with time-varying XBT and MBT depth bias corrections, J. Oceanogr., 65, 287–299, 2009. 4226, 4229

Jevrejeva, S., Moore, J., Grinsted, A., and Woodworth, P.: Recent global sea level acceleration started over 200 years ago, Geophys. Res. Lett., 35, L08715, doi:10.1029/2008GL033611, 2008a. 4228, 4232, 4257

Jevrejeva, S., Moore, J. C., and Grinsted, A.: Relative importance of mass and volume changes to global sea level rise, J. Geophys. Res., 113, D08105, doi:10.1029/2007JD009208, 2008b. 4233

Katsman, C. and van Oldenborgh, G.: Tracing the upper ocean's "missing heat", Geophys. Res. Lett., 38, L14610, doi:10.1029/2011GL048417, 2011. 4225

Kemp, A., Horton, B., Donnelly, J., Mann, M. E., Vermeer, M., and Rahmstorf, S.: Climate related sea-level variations over the past two millennia, P. Natl. Acad. Sci., 108, 11017–11022, doi:10.1073/pnas.1015619108, 2011. 4229, 4233, 4257

Knight, J. R., Allan, R. J., Folland, C. K., Vellinga, M., and Mann, M. E.: A signature of persistent natural thermohaline circulation cycles in observed climate, Geophys. Res. Lett., 32, L20708, doi:10.1029/2005GL024233, 2005. 4241

Legutke, S. and Voss, R.: The Hamburg Atmosphere-Ocean Coupled Circulation Model ECHO-G, Tech. Rep. 18, DKRZ, Hamburg, Germany, 1999. 4227

Levitus, S., Antonov, J. I., Wang, J., Delworth, T. L., Dixon, K. W., and Broccoli, A. J.: Anthropogenic Warming of Earth's Climate System, Science, 292, 267–270, 2001. 4225

Levitus, S., Antonov, J., Boyer, T., Garcia, H. E., and Locarnini, R. A.: EOF analysis of upper ocean heat content, 1956–2003, Geophys. Res. Lett., 32, L18607, doi:10.1029/2005GL023606, 2005. 4225

Levitus, S., Antonov, J. I., Boyer, T., Locarnini, R., Garcia, H., and Mishonov, A.: Global ocean heat content 1955–2008 in light of recently revealed instrumentation problems, Geophys. Res. Lett., 36, L07608, doi:10.1029/2008GL037155, 2009. 4226, 4229

Levitus, S., Antonov, J., Boyer, T. P., Baranova, O. K., Garcia, H. E., Locarnini, R. A., Mishonov, A., Reagan, J. R., Seidov, D., Yarosh, E. S., and Zweng, M. M.: World ocean heat content and thermosteric sea level change (0–2000 m), 1955–2010, Geophys. Res. Lett., 39, L10603, doi:10.1029/2012GL051106, 2012. 4228

Lyman, J. M., Good, S. A., Gouretski, V. V., Ishii, M., Johnson, G. C., Palmer, M. D., Smith, D. M., and Willis, J. K.: Robust warming of the global upper ocean, Nature, 465, 334–337, doi:10.1038/nature09043, 2010. 4225, 4229

Mantua, N., Hare, S., Zhang, Y., Wallace, J., and Francis, R.: A pacific interdecadal climate oscillation with impacts on salmon production, B. Am. Meteorol. Soc., 78, 1069–1080, 1997. 4239

Meehl, G. A., Stocker, T. F., Collins, W. D., Friedlingstein, P., Gaye, A. T., Gregory, J. M., Kitoh, A., Knutti, R., Murphy, J. M., Noda, A., Raper, S. C. B., Watterson, I. G., Weaver, A. J., and Zhao, Z. C.: Global Climate Projections, in Climate Change 2007: The Physical Science Basis. Contribution of Working Group I to the Fourth Assessment Report of the Intergovernmental Panel on Climate Change, Cambridge University Press, Cambridge, United Kingdom and New York, NY, USA, 2007. 4234

Meehl, G., Arblaster, J., Fasullo, J., Hu, A., and Trenberth, K. E.: Model-based evidence of deep-ocean heat uptake during surface-temperature hiatus periods, Nature Climate Change, 1, 360–364, doi:10.1038/NCLIMATE1229, 2011. 4225

Miller, L. and Douglas, B. C.: Mass and volume contributions to twentieth-centur global sea level rise, Nature, 428, 406–409, 2004. 4233

Nakicenovic, N., Alcamo, J., Davis, G., de Vries, B., Fenhann, J., Gaffin, S., Gregory, K., Grubler, A., Jung, T. Y., Kram, T., Rovere, E. L. L., Michaelis, L., Mori, S., Morita, T., Pepper, W., Pitcher, H., Price, L., Riahi, K., Roehrl, A., Rogner, H. H., Sankovski, A., Schlesinger, M., Shukla, P., Smith, S., Swart, R., van Rooijen, S., Victor, N., and Dadi, Z.: Special Report on Emissions Scenarios, Cambridge University Press, 2002. 4228

Newman, M., Compo, G., and Alexander, M.: ENSO-forced variability of the Pacific decadal oscillation, 16, 3853–3857, 2003. 4240

Ortega, P., Montoya, M., González-Rouco, F., Mignot, J., and Legutke, S.: Variability of the Atlantic meridional overturning circulation in the last millennium and two IPCC scenarios, Clim. Dynam., 38, 1925–1947, doi:10.1007/s00382-011-1081-6, 2012. 4226, 4241

Osborn, T. J., Raper, S. C. B., and Briffa, K. R.: Simulated climate change during the last 1000 years: comparing the ECHO-G general circulation model with the MAGICC simple climate model, Clim. Dynam., 27, 185–197, doi:10.1007/s00382-006-0129-5, 2006. 4227, 4228

Palmer, M. D., Good, S. A., Haines, K., Rayner, N. A., and Stott, P. A.: A new perspective on warming of the global oceans, Geophys. Res. Lett., 36, L20709, doi:10.1029/2009GL039491, 2009. 4225

Palmer, M. D., Mcneall, D. J., and Dunstone, N. J.: Importance of the deep ocean for estimating decadal changes in earth's radiation balance, Geophys. Res. Lett., 38, L13707, doi:10.1029/2011GL047835, 2011. 4231

Pickart, R. S., Spall, M. A., Ribergaard, M. J., Moore, G. W. K., and Milliff, R. F.: Deep convection in the Irminger Sea forced by the Greenland tip jet, Nature, 424, 152–156, 2003. 4239, 4240

Roeckner, E., Arpe, K., Bengtsson, L., Christoph, M., Claussen, M., Dumenil, L., Esch, M., Giorgetta, M., Schlese, U., and Schulzweida, U.: The atmospheric general circulation model ECHAM4: model description and simulation of present-day climate. Tech. Rep. 218, Max-Planck-Institut fuer Meterologie, Hamburg, Germany, 1996. 4227

Schmidt, G. A., Jungclaus, J. H., Ammann, C. M., Bard, E., Braconnot, P., Crowley, T. J., Delaygue, G., Joos, F., Krivova, N. A., Muscheler, R., Otto-Bliesner, B. L., Pongratz, J., Shindell, D. T., Solanki, S. K., Steinhilber, F., and Vieira, L. E. A.: Climate forcing reconstructions for use in PMIP simulations of the last millennium (v1.0), Geosci. Model Dev., 4, 33–45, doi:10.5194/gmd-4-33-2011, 2011. 4228

Schmittner, A., Latif, M., and Schneider, B.: Model projections of the North Atlantic thermohaline circulation for the 21st century assessed by observations, Geophys. Res. Lett., 32, L23710, doi:10.1029/2005GL024368, 2005. 4231

Swingedouw, D., Mignot, J., Braconnot, P., Mosquet, E., Kageyama, M., and Alkama, R.: Impact of freshwater release in the north atlantic under different climate conditions in an oagcm, J. Climate, 22, 6377–6403, 2009. 4225

Torrence, C. and Webster, P.: Interdecadal changes in the enso-monsoon system, J. Climate, 12, 2679–2690, 1999. 4237

Trenberth, K.: The definition of El Niño, B. Am. Meteorol. Soc., 78, 2771–2778, 1997. 4239

Trenberth, K.: The ocean is warming, isn't it?, Nature, 465, p. 304, doi:10.1038/465304a, 2010. 4225

Trenberth, K. and Fasullo, J. T.: Tracking earth's energy, Science, 328, 316–317, doi:10.1126/science.1187272, 2010. 4225

Wallace, J. and Gutzler, D.: Teleconnections in the geopotential height field during the Northern Hemisphere winter, Mon. Weather Rev., 109, 784–812, 1981. 4239

Willis, J., Roemmich, D., and Cornuelle, B.: Interannual variability in upper ocean heat content, temperature, and thermosteric expansion on global scales, J. Geophys. Res., 109, C12036, doi:10.1029/2003JC002260, 2004. 4225, 4239

Wolff, J. O., Maier-Reimer, E., and Legutke, S.: The Hamburg Ocean Primitive Equation Model, Tech. Rep. 13, DKRZ, Hamburg, Germany, 1997. 4227

Zhang, Y., Wallace, J., and Battisti, D. S.: ENSO-like interdecadal variability: 1900–93, J. Climate, 10, 1004–1020, 1997. 4239

Zorita, E., von Storch, H., González-Rouco, F. J., U Cubasch, J. L., Legutke, S., Fischer-Bruns, I., and Schlese, U.: Climate evolution in the last five centuries simulated by an atmosphere-ocean model: global temperatures, the North Atlantic Oscillation and the Late Maunder Minimum, Meteorol. Z., 13, 271–289, 2004. 4228

Table 1. Percentage of OHC variance explained by the total equivalent radiative forcing during the periods 1955–2010, 1955–1990 and 1991–2010. This fraction of variance is calculated for the whole ocean and also individually for the three major basins.

		World Ocean	Pacific Ocean	Indian Ocean	Atlantic Ocean
1955–2010	OBS	68 %	67 %	42 %	63 %
	FOR1 + A2	69 %	66 %	66 %	70 %
	FOR1 + B2	67 %	63 %	68 %	64 %
1955–1990	OBS	33 %	32 %	20 %	11 %
	FOR1	12 %	4 %	22 %	14 %
	FOR2	23 %	23 %	27 %	4 %
1991–2010	OBS	84 %	61 %	69 %	76 %
	A2	99 %	98 %	90 %	97 %
	B2	99 %	95 %	86 %	95 %

CPD
8, 4223–4267, 2012

CPD
8, 4223–4267, 2012

Table 2. Linear trends of the ocean heat content in the upper 700 m (in 10^{22} J yr^{-1}) during the periods 1955–1990 and 1991–2010 in the World ocean, and the three main basins.

		World Ocean	Pacific Ocean	Indian Ocean	Atlantic Ocean
1955–1990	OBS	0.11	0.03	0.02	0.06
	FOR1	0.24	0.09	0.05	0.10
	FOR2	0.26	0.11	0.07	0.08
1991–2010	OBS	0.57	0.20	0.14	0.23
	A2	0.86	0.36	0.25	0.25
	B2	0.72	0.30	0.17	0.26

Table 3. Linear trends in sea level (in $mm\,yr^{-1}$) and thermal expansion (in $mm\,yr^{-1}$) for the whole ocean in the periods 1955–2000, 1800–2000 and 2000–2100.

	Thermal expansion				Sea Level Rise
	OBS	FOR1	FOR1 + A2	FOR1 + B2	Jev08
1800–2000		0.24	0.24	0.24	1.38
1955–2000	0.26	0.46	0.53	0.52	1.55
2000–2100			1.78	1.41	

CPD
8, 4223–4267, 2012

Ocean heat content during the last millennium

P. Ortega et al.

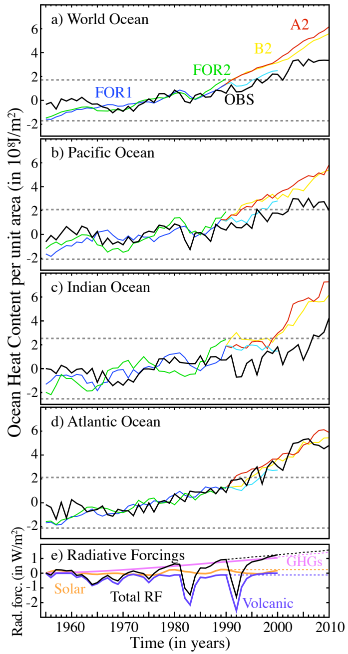

Fig. 1. **(a–d)** Evolution of OHC anomalies normalised per unit area (in $10^8\,\mathrm{J\,m^{-2}}$) in the upper 700 m of the World ocean and the three main ocean basis. Observed OHC (OBS) is calculated from temperature profiles of the Ocean Climate Laboratory at NODC. Simulated OHC anomalies are computed for the forced simulations FOR1 and FOR2 from 1955 to 1990, and for the scenario runs A2 and B2 from 1991 to 2010. FOR1 has been extended to year 2000 (light blue line), thus also incorporating Pinatubo's eruption. Horizontal dashed lines represent a threshold of ±2 standard deviations from the long-term variability in CTRL. The reference period for the anomalies is 1960–1990. **(e)** Estimates of the radiative forcings expressed as changes with respect to year 1955. Dotted lines correspond to projections of the radiative forcing in the A2 scenario run.

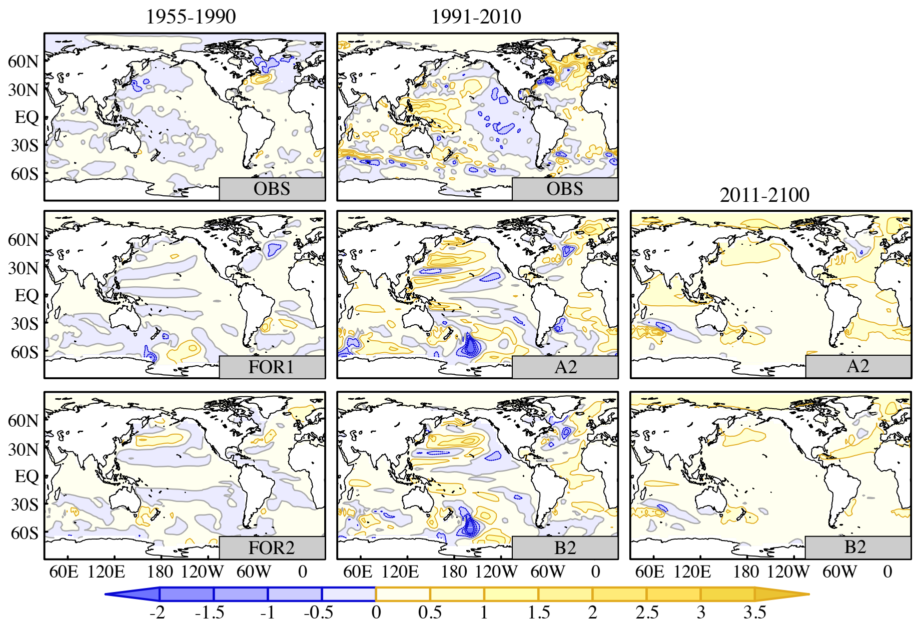

Fig. 2. Linear trends of the observed (top panel) and simulated (lower panels) OHC (in $10^8\,\mathrm{J\,m^{-2}\,yr^{-1}}$) in the upper 700 of the ocean for the periods 1955–1990 (left), 1991–2010 (middle) and 2011–2100 (right).

CPD
8, 4223–4267, 2012

Ocean heat content during the last millennium

P. Ortega et al.

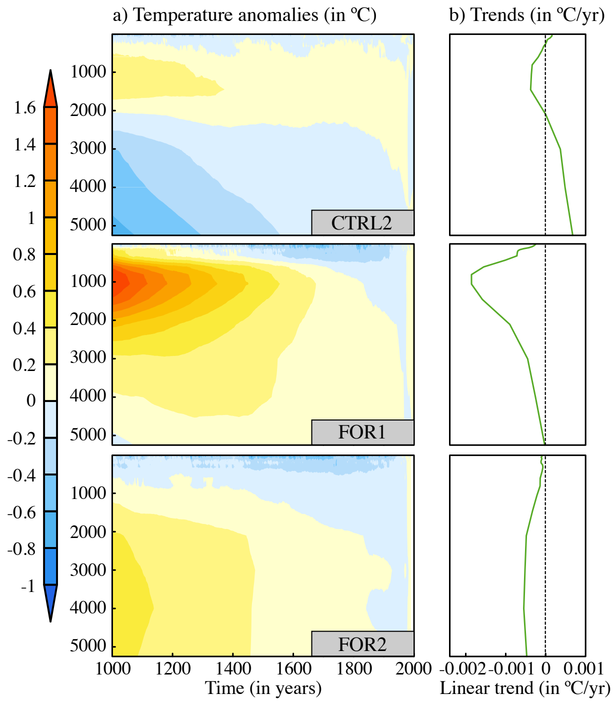

Fig. 3. **(a)** Hovmoller plot (depth vs. time) of the anomalous global temperature (in °C) for CTRL, FOR1 and FOR2. The reference period is 1960–1990. **(b)** Long-term trends of the ocean temperature means at different depths.

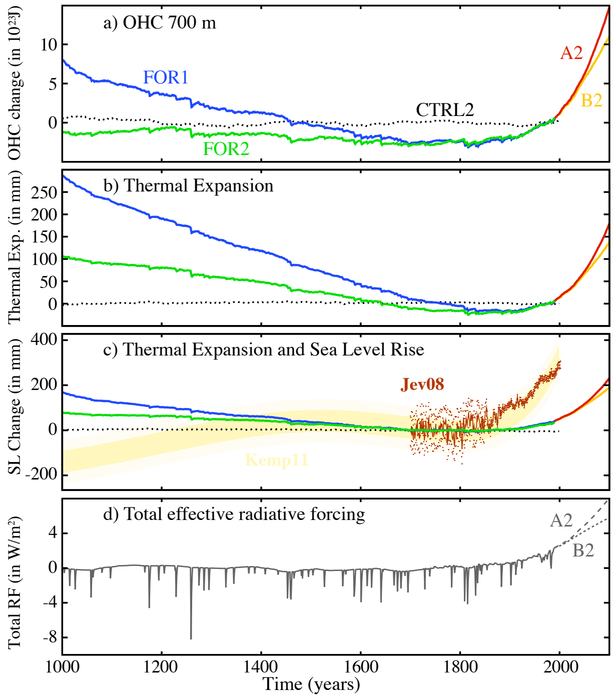

Fig. 4. (a) Anomalies of global ocean heat content in the upper 700 m (in 10^{23} J) wrt the period 1960–1990; **(b)** anomalies of the thermal expansion in the whole depth of the ocean (in mm) for the same period; **(c)** detrended thermal expansion anomalies wrt the period 1700–1800 (see text for details); **(d)** effective radiative forcing applied to the forced simulations (in W m^{-2}). For comparison, sea level rise changes estimated from tide gauges (brown line; Jevrejeva et al., 2008a) and an idealized summary curve from proxy reconstructions with salt-marsh sediments in North Carolina (yellow filled curve; Kemp et al., 2011).

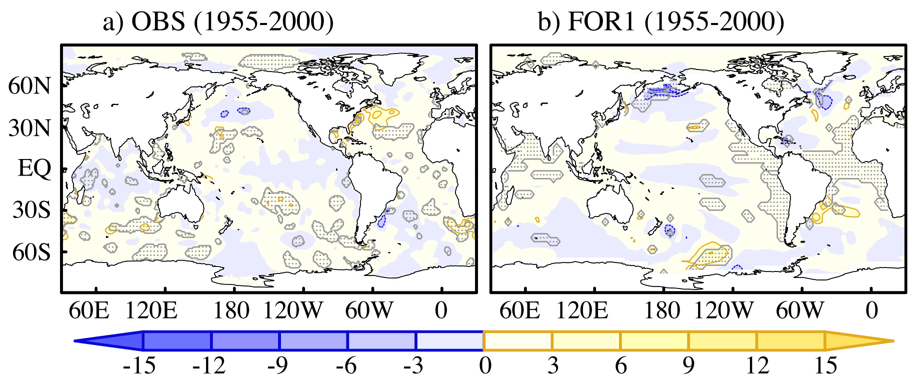

Fig. 5. Regression patterns between the OHC700 anomalies (in $10^8\,\mathrm{J\,m^{-2}}$) and the standardised total radiative forcing in Fig. 1 during the period 1955–2000 of: **(a)** the observations, **(b)** the extended FOR1 run. Dotted areas enclose values significant at a 0.05 % level according to a Student's t-test that takes into account the series autocorrelation to correct the sample size.

CPD
8, 4223–4267, 2012

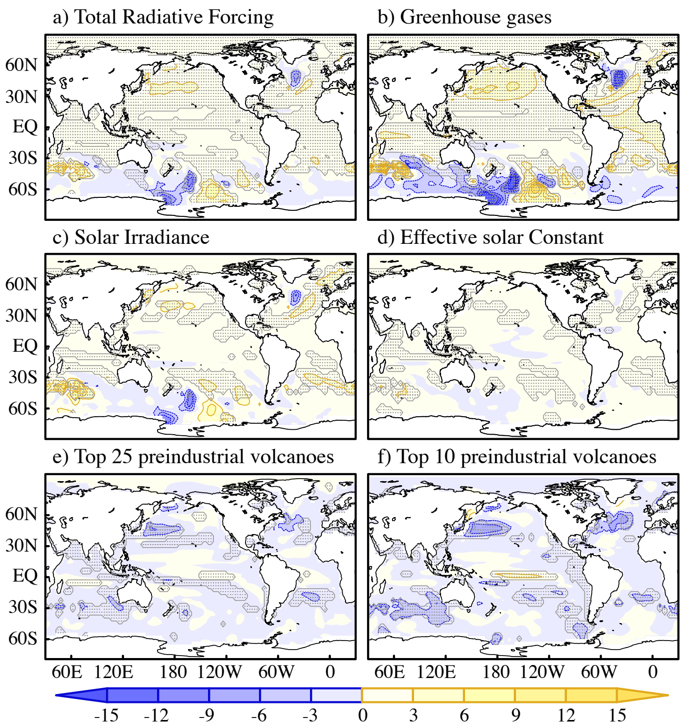

Fig. 6. (a–d) Regression patterns in FOR2 between the OHC700 anomalies (in $10^8\,\mathrm{J\,m^{-2}}$) and the standardised series of the total radiative forcing, the equivalent forcing of GHGs, the solar irradiance and the effective solar constant, respectively. Significance is addressed as in Fig. 5. **(e–f)** Composite of the OHC700 differences between the 5 yr following and 5 yr preceding the top 10 and 25 largest preindustrial eruptions. Significance is established at the 0.05 level through a Monte Carlo test based on 1000 random selections in CTRL.

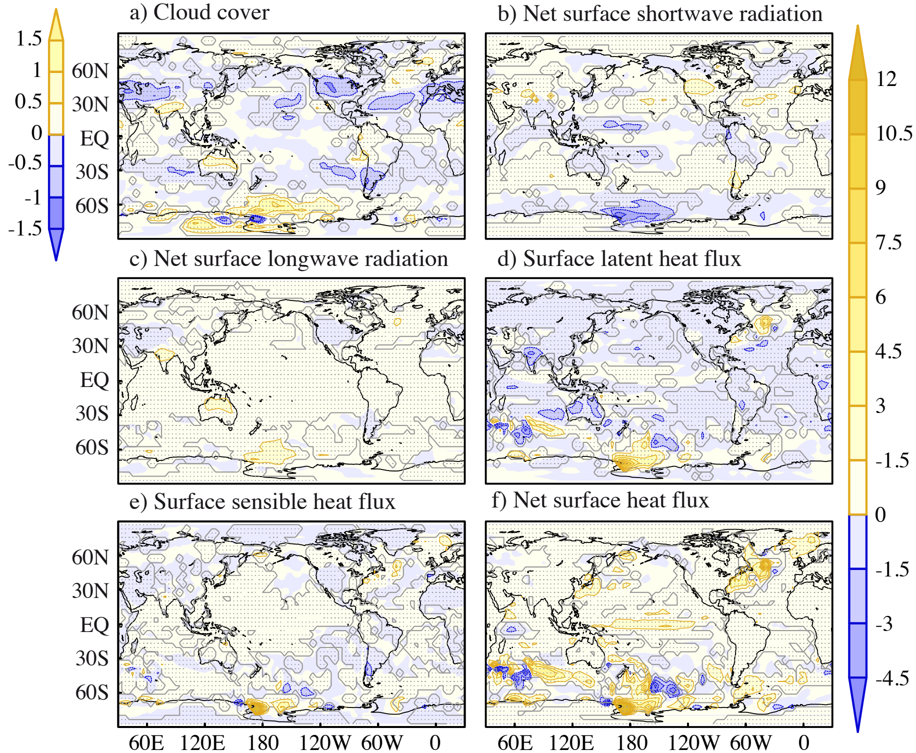

Fig. 7. In-phase regression patterns in FOR2 between the standardised total radiative forcing and **(a)** the total cloud cover (in %), **(b–f)** the different components of the net surface heat flux (in $W\,m^{-2}$).

CPD
8, 4223–4267, 2012

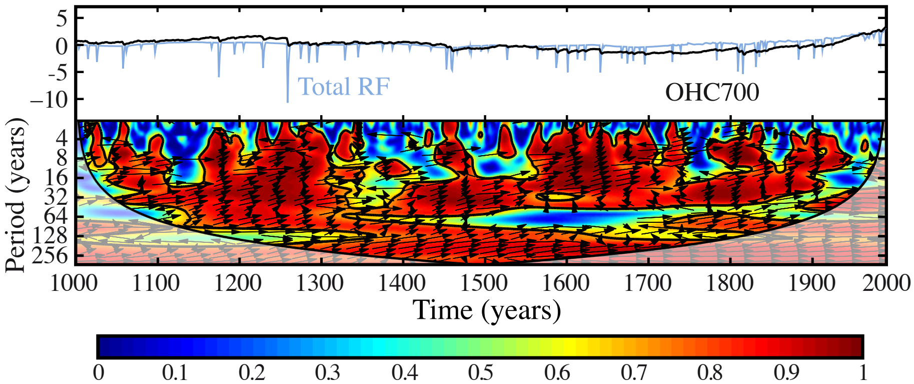

Fig. 8. Top: standardised time series of the total radiative forcing and the OHC700 changes in the FOR2 simulation. Bottom: squared wavelet coherence between both time series. The black contours enclose areas where the coherence is significant at a 5 % level according to a Monte Carlo test. The arrows indicate the phase of their interrelationship (eastward arrows account for phase zero). Note that positive phases (represented by northward arrows) correspond to the forcing leading the OHC700 changes. The cone of influence (thick black curve) accounts for the region the edge effects become important. The horizontal dotted line highlights the frequency corresponding to a 10 yr timescale.

CPD
8, 4223–4267, 2012

Ocean heat content during the last millennium

P. Ortega et al.

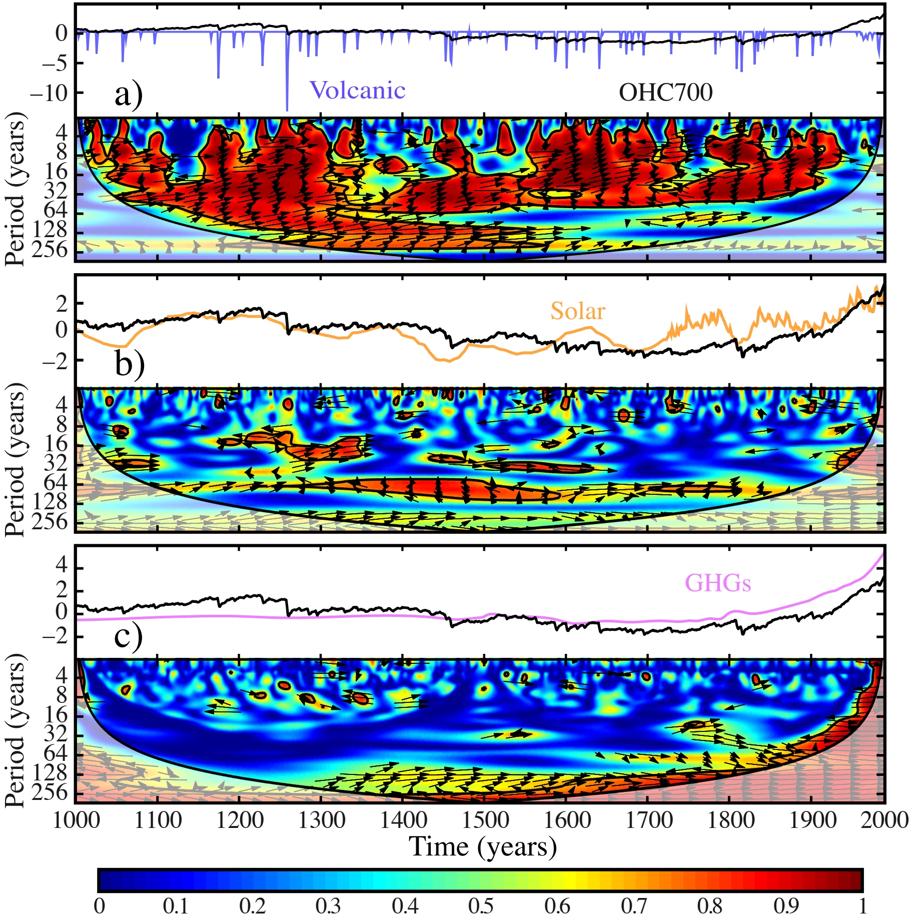

Fig. 9. The same as in Fig. 8 but for OHC700 and the standardised series of: **(a)** volcanic forcing; **(b)** solar irradiance; **(c)** effective GHG forcing.

CPD
8, 4223–4267, 2012

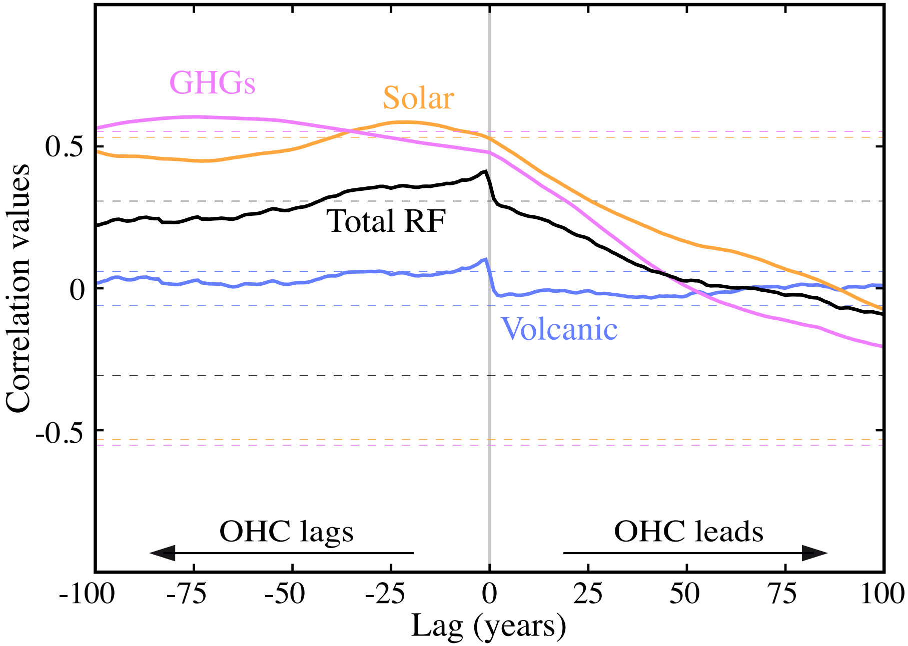

Fig. 10. Time-lag correlations in FOR2 between the OHC700 changes and the different radiative forcings. The thin colored horizontal lines represent the threshold value for significance associated with each forcing. Significance is assessed as in Fig. 5.

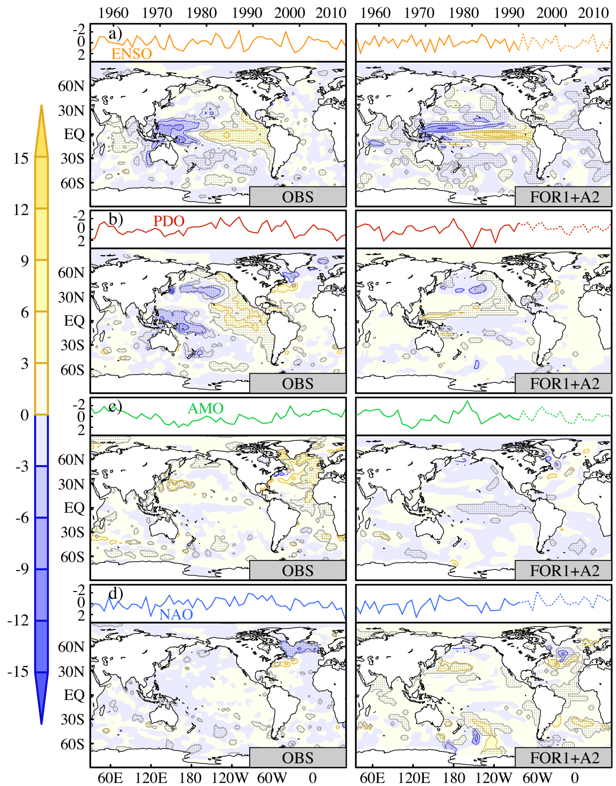

Fig. 11. Top: Observed (left) and simulated (right) standardised indices of: **(a)** niño3.4; **(b)** PDO; **(c)** AMO; **(d)** NAO. See text for details on the particular definitions applied. Dashed lines correspond to projections in the A2 scenario run. Bottom: regression patterns between the anomalies of OHC700 (in $10^8\,\mathrm{J\,m^{-2}}$) and the indices above. Significance is addressed as in Fig. 5.

CPD
8, 4223–4267, 2012

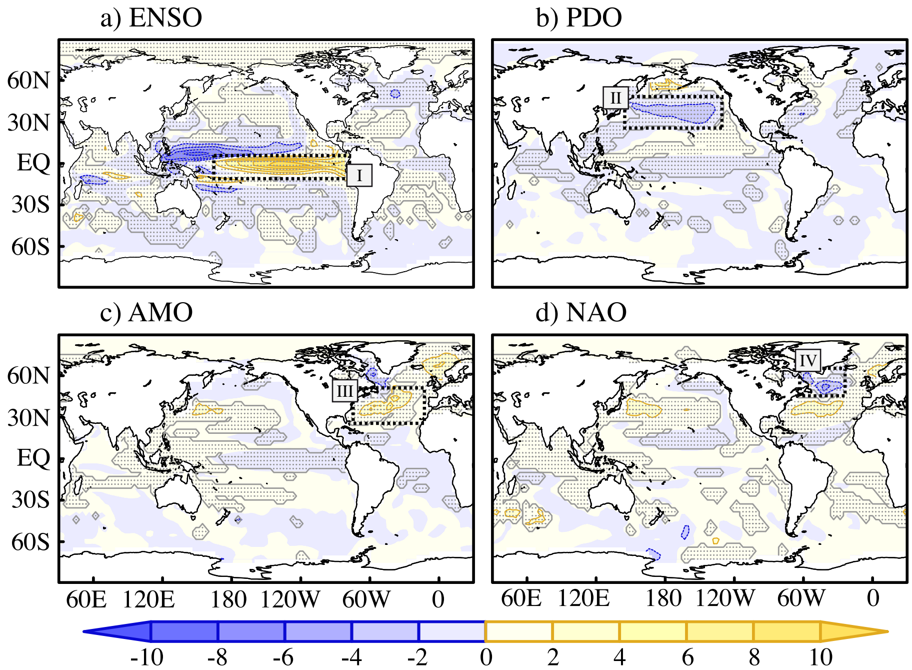

Fig. 12. Regression patterns between the OHC700 anomalies (in $10^8\,\mathrm{J\,m^{-2}}$) and the standardised indices in the whole FOR2 simulation: **(a)** niño3.4; **(b)** PDO; **(c)** AMO; **(d)** NAO. Significance is addressed as in Fig. 5. The black dotted rectangles delimit the regions assessed in the wavelet coherence analysis of Fig. 14. Boxes are defined for each climate index to average the OHC700 anomalies over the regions where their fingerprint is larger.

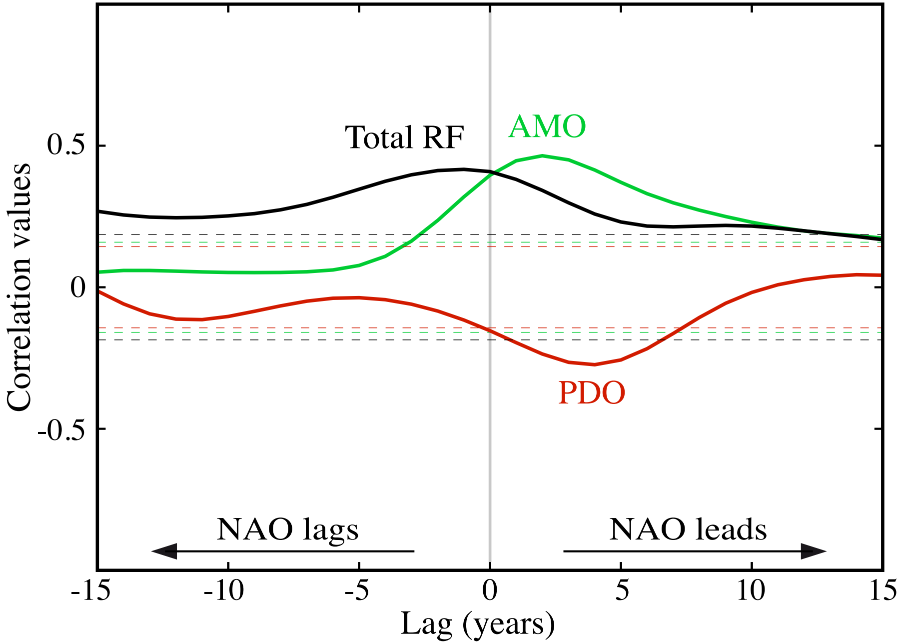

Fig. 13. Time-lag correlations between the decadally filtered indices of the NAO and the following timeseries: the PDO (red line), the AMO (green line) and the total radiative forcing (black line). The thin colored horizontal lines represent the threshold value for significance associated with each series. Significance is addressed as in Fig. 5.

CPD
8, 4223–4267, 2012

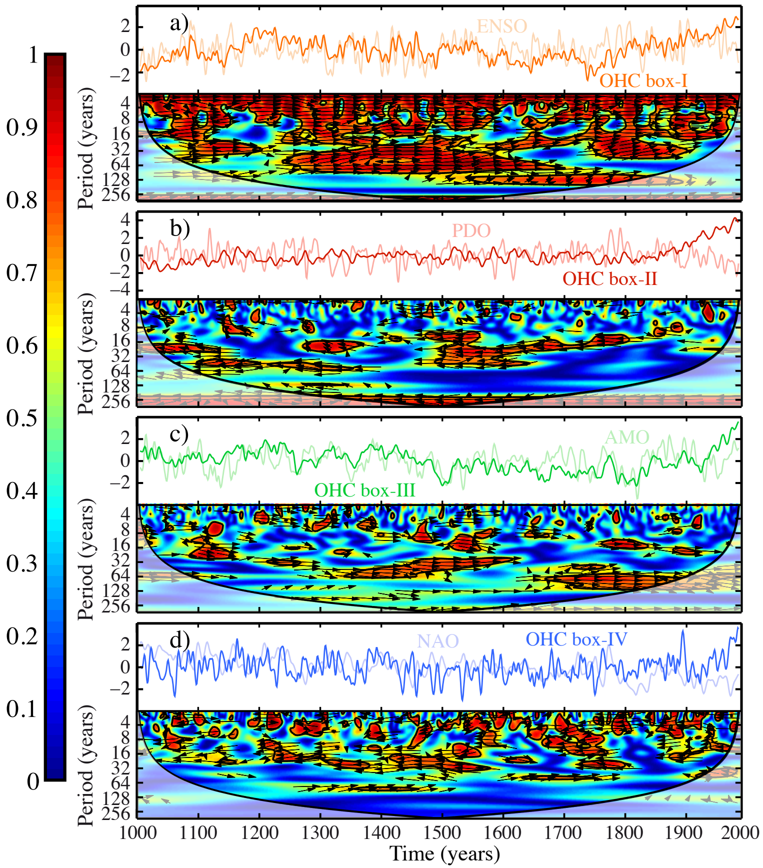

Fig. 14. The same as in Fig. 8 but between the standardised indices of ENSO, PDO, AMO and NAO and the OHC700 averages in the corresponding boxes defined in Fig. 12. In the top panels timeseries are detrended decadally to ease comparison at interdecadal timescales.

CPD
8, 4223–4267, 2012